Remote Sensing of Environment 282 (2022) 113297

Contents lists available at ScienceDirect

Remote Sensing of Environment

journal homepage: www.elsevier.com/locate/rse

Integrated coastal subsidence analysis using InSAR, LiDAR, and land cover data

Wen Zhong [a,b], Tianxing Chu [a,b], Philippe Tissot [a], Zhenming Wu [c], Jie Chen [d], Hua Zhang [e,*]

[a] Conrad Blucher Institute for Surveying and Science, Texas A&M University-Corpus Christi, Corpus Christi, TX 78412, USA
[b] Department of Computing Sciences, College of Science and Engineering, Texas A&M University-Corpus Christi, Corpus Christi, TX 78412, USA
[c] Department of Meteorology, University of Reading, Reading, Berkshire RG6 6BB, UK
[d] State Key Laboratory of Cryospheric Science, Northwest Institute of Eco-Environment and Resources, Chinese Academy of Sciences, Lanzhou 730000, China
[e] Department of Engineering, College of Science and Engineering, Texas A&M University-Corpus Christi, Corpus Christi, TX 78412, USA

ARTICLE INFO

Edited by Jing M. Chen

Keywords:
Land subsidence
Coastal regions
InSAR
Airborne LiDAR
Land cover

ABSTRACT

Land subsidence is an important cause of relative sea-level rise along the Gulf Coast. There is a lack of effective monitoring of coastal subsidence with high accuracy and high spatial resolution for improving coastal risk assessment and mitigation. This study is the first attempt to integrate satellite interferometric synthetic aperture radar (InSAR) and airborne light detection and ranging (LiDAR) methods to investigate the spatiotemporal pattern of coastal subsidence. The study area is around Eagle Point, Texas, a region known for its fast rate of relative sea-level rise in recent decades. From 2006 to 2011, the line-of-sight velocities were up to −33 mm/year based on ascending ALOS-1 PALSAR-1 images. From 2016 to 2021, the vertical velocities were up to −34 mm/year based on ascending and descending Sentinel-1 images. Additional details of the subsidence pattern were revealed by incorporating the surface difference derived from 1-m airborne LiDAR results. Comparisons of the InSAR-derived velocities from image time series and the LiDAR-derived surface changes from time-lapsed observations were conducted at different spatial levels with linkages to land cover patterns and topography. The results showed that local subsidence rates could vary significantly below the spatial resolution of InSAR results, indicating a valuable role of airborne LiDAR results in extending InSAR results to parcel and building levels and explaining subpixel uncertainties. Also, subsidence appeared to be stronger in vegetated areas than in developed areas and negatively correlated with surface imperviousness. The magnitude of subsidence was not correlated with elevation along selected transect lines. Overall, this study demonstrated the benefits of combining InSAR results with other geospatial datasets to characterize coastal subsidence. In particular, the high vertical accuracy of InSAR results and the high spatial resolution of airborne LiDAR results could be complementary, highlighting the necessity of multi-resolution data fusion to support studies on coastal flood vulnerability, infrastructure reliability, and erosion control.

1. Introduction

Over 600 million people, or 10% of the world's population, live in low-lying coastal areas below 10 m in elevation (Neumann et al., 2015). These coastal areas are unique ecosystems that offer habitats for many species and provide essential services to human society. The market value of marine and coastal resources was estimated at $3 trillion annually as the year of 2015, accounting for 5% of global gross domestic product (Global Ocean Commission, 2014). Over the past decades, relative sea-level rise (RSLR) has been identified as a significant threat to many coastal areas. It is exacerbating a variety of environmental and ecological problems such as coastal flooding (Ezer and Atkinson, 2014), wetland loss (Schuerch et al., 2018), and coastal erosion (Leatherman et al., 2000), endangering local ecosystems and communities. RSLR is the combined effect of sea-level rise and land subsidence. Potential causes of sea-level rise include meltwater from glaciers and ice sheets, thermal expansion of seawater, and transfer of water from storage on land to sea (Frederikse et al., 2020; Meredith et al., 2019). Land subsidence is associated with natural and human causes at local or regional scales, such as groundwater withdrawal, oil and gas extraction, soil compaction, fault growth, tectonic activities, and other natural processes (Coplin and Galloway, 1999).

* Corresponding author.
E-mail address: hua.zhang@tamucc.edu (H. Zhang).

https://doi.org/10.1016/j.rse.2022.113297
Received 11 March 2022; Received in revised form 22 August 2022; Accepted 26 September 2022
Available online 8 October 2022

The contribution of land subsidence to RSLR is particularly significant along the Texas Gulf Coast (Coplin and Galloway, 1999). For example, the contribution of land subsidence was estimated to be 76–85% of RSLR from 1909 to 1992 and decreased to 30% in 2018 at tide gauge Galveston Pier 21, Texas (Liu et al., 2020), over an area known for significant subsidence (Miller and Shirzaei, 2019; Qu et al., 2015). Driven by growing concerns about the effect of land subsidence on coastal flooding, shoreline erosion, and fault movement (Coplin and Galloway, 1999; Miller and Shirzaei, 2021), there is an urgent need for effective characterization of land subsidence to improve risk management strategies for Texas coastal areas.

Traditional efforts of subsidence analysis rely on ground-based techniques. For example, geodetic surveying methods such as leveling have been used to measure the vertical change of the ground surface at the local scale. Extensometers have also been used to measure aquifer compaction and expansion for estimating subsidence around wells (Huang et al., 2012), but the low spatial coverage of extensometers hinders the understanding of the spatial variations of regional subsidence. Another method for subsidence monitoring is the global navigation satellite system (GNSS) (Wang et al., 2017). In particular, continuous GNSS stations, such as NOAA's continuously operating reference station (CORS) network, can offer positioning observations with high accuracy, but the results are only valid for a limited area around the stations.

Geodetic remote sensing techniques can continuously monitor the dynamic displacement of the ground surface and provide a new means to quantify land subsidence. In particular, the interferometric synthetic aperture radar (InSAR) has been proven to be an effective tool to map land subsidence with centimeter-to-millimeter accuracy over a large geospatial extent (Bürgmann et al., 2000). It compares two or more synthetic aperture radar (SAR) images that are collected at different times over the same region to quantify the change of ground surface. Due to the growing availability of high-quality SAR datasets, InSAR has been increasingly used in coastal subsidence studies (Dixon et al., 2006; Wang et al., 2012). For example, Qu et al. (2015) mapped the line-of-sight (LOS) subsidence in the Galveston-Houston region, Texas, using InSAR based on ERS, Envisat ASAR, and ALOS-1 PALSAR-1 images from 1993 to 2011. Miller and Shirzaei (2021) generated the vertical land subsidence rates over this area based on ALOS-1 PALSAR-1 and Sentinel-1 images between 2007 and 2019 and GNSS measurements which provided the horizontal components of the motion for the same period. Results of these InSAR-based subsidence studies typically have a horizontal spatial resolution in tens-of-meters. In comparison, airborne light detection and ranging (LiDAR) could offer insights at a higher spatial resolution (up to 1 m), although with a lower absolute vertical accuracy (10–15 cm). Airborne LiDAR is an aerial mapping technology that integrates LiDAR and aerial platforms (e.g., a drone, plane, or helicopter) to collect the three-dimensional (3D) point cloud of the earth's surface for the generation of a digital terrain model (DTM) or digital elevation model (DEM). Recent advances in drone technology have particularly promoted the applications of airborne LiDAR. Integrating InSAR and airborne LiDAR methods can potentially study coastal subsidence with high accuracy and high spatial resolution.

The objectives of this study are to 1) quantify the subsidence rates in a Texas coastal area from 2006 to 2021 using the small baseline subset (SBAS) InSAR method, and 2) compare the InSAR results to the high-resolution land surface differences derived from multitemporal airborne LiDAR data, and 3) investigate the relationships between subsidence and the patterns of land cover and topography. This study aims to explore a complementary relationship between the high accuracy InSAR results and the high spatial resolution airborne LiDAR results in supporting coastal subsidence studies.

2. Study area

The study area is a 520 km^2 area around Eagle Point in Texas, located between 29°20′N and 29°34′N and between 95°5′W and 94°52′W (Fig. 1). The land cover is dominated by a mixture of coastal prairie, urban areas, and an industrial zone of oil and gas facilities in the southeast area. Elevation ranges from −4.43 m to 17.05 m with an average slope of 0.18°. Records from the Eagle Point Tide Gauge Station show an RSLR rate of 13.7 mm y^{-1} from 1993 to 2017 (Fig. 1b). A possible cause is the withdrawal of groundwater from the Chicot, Evangeline, and Jasper aquifers, all components of a broader Gulf Coast aquifer system, to meet the increasing industrial and municipal water demands from the Galveston area. Oil and gas extraction, and surface fault activities could also contribute to the land subsidence here (Coplin and Galloway, 1999; Qu et al., 2015).

3. Methods and materials

3.1. Overview

This study combined InSAR, airborne LiDAR, GPS, and land cover data to investigate the spatiotemporal pattern of coastal land subsidence and its relation to different land cover and topography, consisting of several steps (Fig. 2). First, three stacks of SAR images were used to obtain the LOS subsidence velocities, i.e., two orbits from Sentinel-1 and one from ALOS-1 PALSAR-1. LOS velocities in Sentinel-1 ascending and descending geometries were utilized then to generate the projections onto the vertical and east-west horizontal directions under the assumption of zero north-south motion. Second, this study generated a 1-m map of land surface differences from two temporal airborne LiDAR point cloud data to compare and complement InSAR results. Third, the InSAR results were overlapped with land cover data to examine the occurrence of subsidence in different land cover categories, and its relationship with percent surface imperviousness. Finally, InSAR results and LiDAR DEM were combined in a profile analysis to investigate the pattern of subsidence along selected typical transections and highways across the study area. Highways are often a focus of mitigation and response studies for flooding risk management, as land subsidence along low-lying highway sections could exacerbate the inundation risk.

3.2. InSAR-based subsidence analysis

3.2.1. SAR images

This study used two sets of SAR data (Table 1). The L-band ALOS-1 PALSAR-1 data included 26 ascending images taken between December 2006 and January 2011. The descending PALSAR-1 data over the study area was limited and not adopted in this study. Therefore, we analyzed the LOS velocities based on these ascending PALSAR-1 images. The PALSAR-1 raw data were provided by Japan Aerospace Exploration Agency (JAXA). The C-band Sentinel-1 SAR data included 252 ascending and descending images between April 2016 and September 2021. Combining ascending and descending Sentinel-1 images allowed for calculating vertical and east-west horizontal components of LOS velocities under the assumption of zero north-south components (Eq. (1–5)). Most SAR satellites, such as ALOS and Sentinel-1, operate in a sun-synchronous orbit with an inclination of around 98°, resulting in range observations almost in the east-west direction and rarely in the north-south direction. Consequently, the north-south components cannot be extracted adequately from these SAR data-derived LOS velocities (Wright et al., 2004). Using Sentinel-1 images till 2021 other than till 2018 (the same end year with airborne LiDAR data) would provide a more comprehensive understanding of the subsidence pattern for our study area. The Sentinel-1 single look complex (SLC) data were provided by the Copernicus program of the European Space Agency. Full details of the SAR data are presented in Supplementary Information.

3.2.2. SBAS InSAR analysis

We used the SBAS method to retrieve historical subsidence from SAR images. The SBAS method utilizes interferograms from small temporal

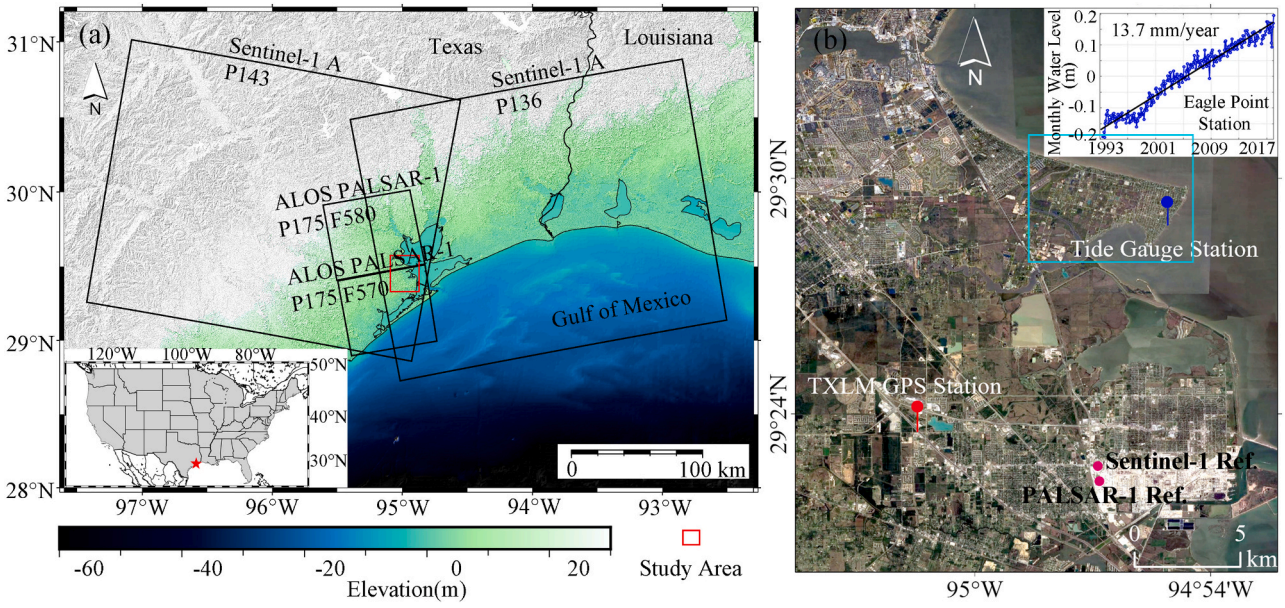

Fig. 1. Study area: (a) SAR data coverage (black squares) over the elevation map around the study area (red square); (b) a Google Earth image of the study area and the monthly mean RSLR observed at the Eagle Point Tide Gauges Station (blue marker) from 1993 to 2017. Red marker shows the location of the TXLM GPS station, and magenta dots denote the location of the reference points for Sentinel-1 and ALOS-1 PALSAR-1 images processing. (For interpretation of the references to colour in this figure legend, the reader is referred to the web version of this article.)

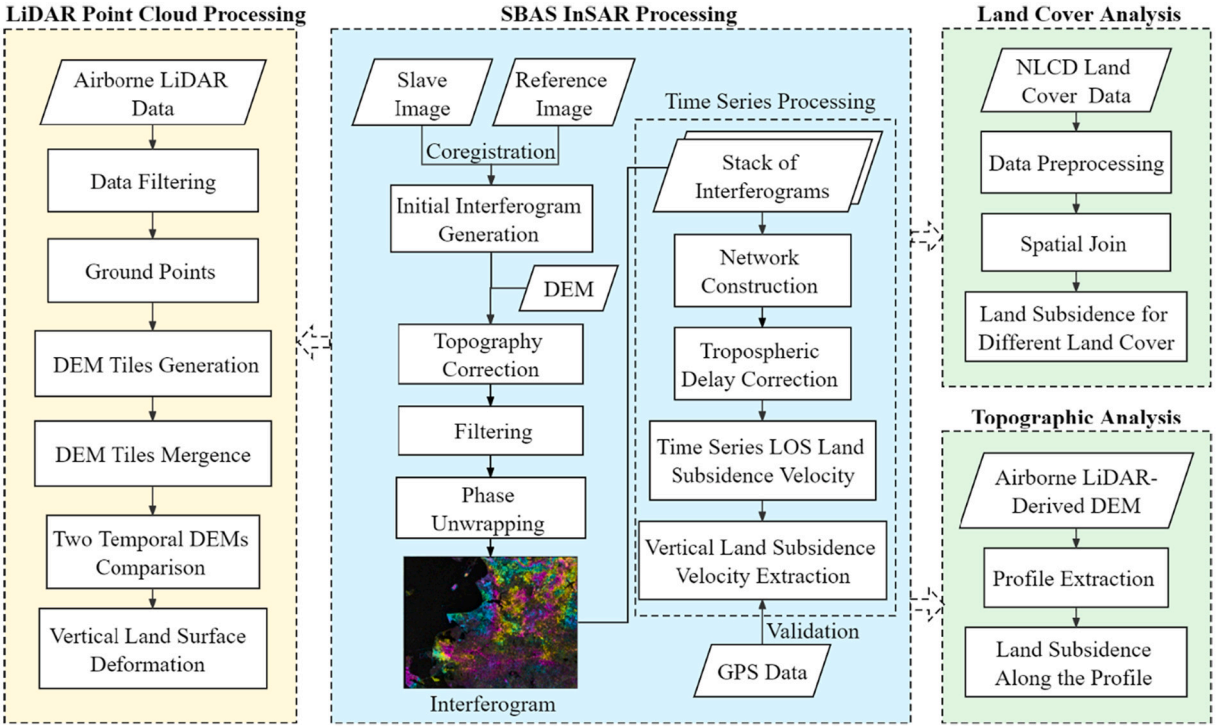

Fig. 2. Research framework.

and spatial baseline subsets, reducing both spatial and temporal decorrelation and improving phase estimates' performance (Berardino et al., 2002). Persistent Scatterer Interferometry (PSI) uses persistent scatterers to obtain the land surface displacements (Ferretti et al., 2001). The persistent scatterers are always substantial in developed urban areas, which renders PSI to be applied more in the urban area. In this study, the study area covers developed urban areas, grassland areas, and wetlands. One of our objectives is investigating the relationship between land subsidence and land cover. SBAS method can overcome the rapid loss of coherence in long-term interferograms in PSI over nonurban areas. So, although PSI can achieve full-resolution (single-look), this study finally applied the SBAS method to map the land subsidence.

For the ALOS-1 PALSAR-1 data, we selected the image collected on 28 March 2008 as the reference image. All other images were coregistered to this reference image. The temporal and perpendicular baseline thresholds for PALSAR-1 data were set as 1200 days and 1500 m,

Table 1
Characteristics of SAR data.

Characteristics \ Sensor	ALOS-1 PALSAR-1	Sentinel-1
Band (Wavelength)	L (23.6 cm)	C (5.6 cm)
Beam mode	FBS, FBD	IW
Revisit time	46 days	12 days
Orbital geometry	Ascending	Ascending/Descending
Path	175	136/143
Frame	570, 580	90–93/491–494
Temporal span	12/2006–1/2011	4/2016–9/2021

respectively (Fig. 3a). For the Sentinel-1 data, the image collected on 10 January 2019 was chosen as the reference image. Interferograms were generated between each epoch and the adjacent four epochs for Sentinel-1 data (Fig. 3b and c). This study used the InSAR Scientific Computing Environment (ISCE) (Rosen et al., 2012) to obtain 49 and 1012 interferograms for PALSAR-1 and Sentinel-1 stacks, respectively. The multilooking approach was leveraged to alleviate the phase noise, which was 9 × 2 (azimuth by range) and 2 × 10 for the PALSAR-1 and Sentinel-1 data, respectively, leading to approximately 30-m pixels. The topographic phase was removed from interferograms using a 30-m Shuttle Radar Topography Mission DEM. In addition, orbit parameters were incorporated to correct orbital errors in Sentinel-1 interferograms generation. All interferograms were unwrapped by adopting the SNAPHU (Statistical-Cost Network-Flow Algorithm for Phase Unwrapping) (Chen and Zebker, 2002).

The Miami InSAR time-series software in Python (MintPy) (Yunjun et al., 2019) was applied to perform the SBAS approach. This study selected the PALSAR-1 interferogram network by utilizing minimum spanning tree (MST) and spatial coherence threshold, i.e., accomplished the MST first by using the inverse of average spatial coherence of all interferograms as weight, then excluded the interferograms that were not included in MST's interferograms and had spatial coherence lower than the threshold. Average spatial coherence thresholds of 0.65 for PALSAR-1 interferograms were applied in this study (Fig. 3a). For the Sentinel-1 interferogram network, the temporal baseline threshold of not exceeding 100 days was applied (Fig. 3b and c). Water bodies were masked out by applying a DEM-based water mask in radar coordinates. We selected two buildings as reference points for PALSAR-1 and Sentinel-1 datasets (magenta dots, denoted as Ref. in Fig. 1b). All interferograms were referenced to the reference point so that the relative LOS velocities can be calculated later. The components of tropospheric delay were removed by ERA5 reanalysis using PyAPS (Python-based Atmospheric Phase Screen estimation) module (Jolivet et al., 2011). This study estimated the LOS velocity as the slope of the best fitting line to the range change time series and the uncertainty of the velocity as the goodness of fit, i.e., standard deviation (Fattahi and Amelung, 2015).

The LOS velocity v_{los} can be decomposed into three velocity components in the east-west direction (v_E), the north-south direction (v_N), and the vertical direction (v_V) (Fialko and Simons, 2001; Wright et al., 2004):

$$v_{los} = \left(-sin\theta cos\alpha \; sin\theta sin\alpha \; cos\theta \right) \begin{pmatrix} v_E \\ v_N \\ v_V \end{pmatrix} \quad (1)$$

where θ is the radar incidence angle and α is the satellite heading angle

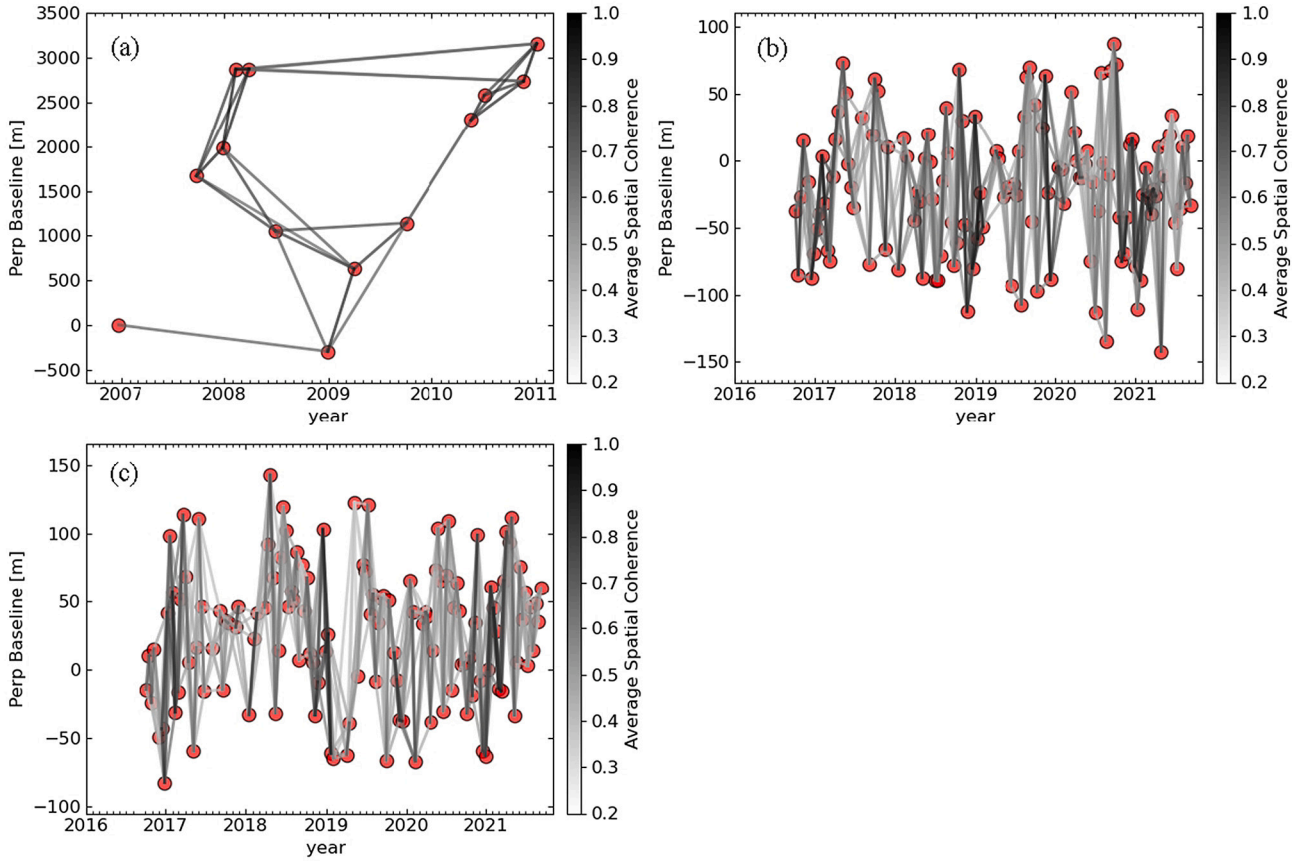

Fig. 3. Interferogram networks from ALOS-1 PALSAR-1 and Sentinel-1 acquisitions with perpendicular and temporal baselines: (a) PALSAR-1 ascending images, (b) Sentinel-1 ascending images, and (c) Sentinel-1 descending images. Red circles represent SAR images. (For interpretation of the references to colour in this figure legend, the reader is referred to the web version of this article.)

(i.e., the direction of the satellite motion). The incidence angle and heading angle are known. In this study, for Sentinel-1 ascending and descending geometries, the mean values for the incidence angles were 32.55° and 32.50°, and the heading angles were 349.22° and 190.79°, respectively. Based on estimated Sentinel-1 ascending LOS velocities v_{los}^{AS} and descending LOS velocities v_{los}^{DS}, Eq. (2) and Eq. (3) can be developed with three unknown velocity components v_E, v_N, and v_V:

$$v_{los}^{AS} = -\sin_{\theta}^{AS} cos_{\alpha}^{AS} v_E + \sin_{\theta}^{AS} \sin_{\alpha}^{AS} v_N + cos_{\theta}^{AS} v_V \quad (2)$$

$$v_{los}^{DS} = -\sin_{\theta}^{DS} cos_{\alpha}^{DS} v_E + \sin_{\theta}^{DS} \sin_{\alpha}^{DS} v_N + cos_{\theta}^{DS} v_V \quad (3)$$

Assuming that the motion in the north-south direction (v_N) is negligible, Eq. (2) and Eq. (3) could be solved to yield the LOS velocity projections onto the vertical (v_V, Eq. (4)) and east-west horizontal direction (v_E, Eq. (5)):

$$v_V = \frac{\sin_{\theta}^{DS} cos_{\alpha}^{DS} v_{los}^{AS} - \sin_{\theta}^{AS} cos_{\alpha}^{AS} v_{los}^{DS}}{cos_{\theta}^{AS} \sin_{\theta}^{DS} cos_{\alpha}^{DS} - \sin_{\theta}^{AS} cos_{\alpha}^{AS} cos_{\theta}^{DS}} \quad (4)$$

$$v_E = \frac{cos_{\theta}^{AS} v_{los}^{DS} - cos_{\theta}^{DS} v_{los}^{AS}}{\sin_{\theta}^{AS} cos_{\alpha}^{AS} cos_{\theta}^{DS} - cos_{\theta}^{AS} \sin_{\theta}^{DS} cos_{\alpha}^{DS}} \quad (5)$$

During the data processing, by inputting Sentinel-1 ascending and descending geometries LOS velocities in the decomposition operation of MintPy, the Sentinel-1 vertical components under the assumption of zero north-south motion could be generated. For the PALSAR-1 ascending geometry used in this study, only Eq. (2) could be developed. With three unknown velocity components, the study estimated the vertical components of PALSAR-1 LOS velocities using Eq. (6). This equation was derived from Eq. (2) by assuming that the east-west and north-south motion were negligible. The mean incidence angle for PALSAR-1 data was 39.7°. This decomposition was executed in the calculation operation of MintPy.

$$v_V = \frac{v_{los}^{AS}}{cos_{\theta}^{AS}} \quad (6)$$

3.2.3. Validation based on GPS data

A CORS GPS station (TXLM) is located in a highly developed area of the study site (Fig. 1b). The GPS data for 2006–2021 were provided by the National Geodetic Survey (NGS) and processed by the Nevada Geodetic Laboratory with respect to the IGS14 reference frame (Blewitt et al., 2018). We used the GPS vertical land surface displacement measurements to validate our InSAR-based subsidence results over an approximately 30 m × 30 m area centered on the GPS station.

3.3. Airborne LiDAR-based land surface difference

We used two airborne LiDAR point cloud datasets of 2006 and 2018, provided by the 3D Elevation Program (3DEP) of the United States Geological Survey (USGS). These datasets' vertical and horizontal datums were NAVD88 and NAD83, respectively. The point density of the 2006 data was below 2 points/m^2 and was deemed adequate to generate a 1-m DEM. 14 categories were classified for the LAS airborne LiDAR point cloud data according to the ASPRS classification standard. This study leveraged the ground class of the point cloud. A standard filtering procedure was applied to extract the bare earth point cloud data (Fig. 2). DEM tiles were generated based on those ground points using the LAStools and were merged then to produce a seamless 1-m DEM. For the 2018 DEM, raw 1-m DEM tiles (1.65 km × 1.85 km) were downloaded from 3DEP and merged into a DEM using QGIS. The airborne LiDAR data in 2018 was offered at level 2 (QL2), which had a minimum nominal pulse spacing (NPS) of 0.7 m and a vertical error of 0.1 m, measured as root mean square error (RMSE). Finally, the land surface differences in the vertical direction between 2006 and 2018 were calculated based on two temporal DEMs using subtraction analysis in QGIS (Fig. 2).

The uncertainties of surface differences were unlikely to be spatially homogeneous, caused by factors such as uncertainties of original DEMs and the error propagation during the change detection. The uncertainties of airborne LiDAR-derived DEM were heterogeneous but always offered as a single value. In this study, the absolute vertical accuracy for QL2 airborne LiDAR data was provided in the USGS report as 0.1 m, but the relative vertical accuracy would be smaller than 0.06 m for smooth surfaces. Quantifying uncertainties in change detection results of airborne LiDAR is not a trivial work and is still very limited (Okyay et al., 2019).

Land surface difference from airborne LiDAR includes the accumulation of gradual land subsidence and land displacements induced by human activities and other surface processes. The periods of airborne LiDAR measurements (2006–2018) had overlaps with that of ALOS-1 PALSAR-1(2006–2011) and Sentinel-1(2016–2021) results. This study compared airborne LiDAR-derived land surface differences to the InSAR-derived velocities. The 1-m map of land surface differences was supposed to complement the PALSAR-1 and Sentinel-1 results by revealing more details of the spatial variations of gradual subsidence below the scale of the 30-m InSAR pixels and identifying the significant land surface change which InSAR cannot capture.

3.4. Subsidence analysis over different coastal land cover and topographic patterns

We obtained the 30-m 2019 land cover from the National Land Cover Database (NLCD). USGS generated the NLCD products through integrating multi-source geospatial datasets and classification using machine learning methods (Jin et al., 2019), and their accuracies were validated at the national level (Wickham et al., 2021).

The land cover analysis was conducted in ArcGIS Pro. First, the NLCD data was extracted and clipped to the same extent as the study area. Then, the NLCD categories were modified to address the land cover pattern of the study area. Deciduous forest, evergreen forest, and mixed forest categories were merged into a forest category. Shrub/scrub, grassland/herbaceous, pasture/hay, and cultivated crops categories were merged into a grassland category. Woody wetlands and emergent herbaceous wetlands categories were merged into a wetlands category. The resulted land cover raster was converted into multi-feature polygons. These polygons were linked to the subsidence estimates using the Spatial Join Tool in ArcGIS Pro. Based on attribute tables of the Spatial Join-derived feature classes, mean subsidence velocities, standard error, and interquartile ranges were calculated for different land cover categories. In addition, linear regression was performed to analyze the relationship between subsidence velocities and surface imperviousness at the pixel level and between mean subsidence velocities and surface imperviousness at the class level.

We further examined the relationship between subsidence and topography using the 2018 airborne LiDAR DEM. The floating-type DEM was first converted into an integer-type DEM and then into polygon features. Next, we established two transect lines (Figure 14a) to represent the dominant elevation gradients over the study area, e.g., transect QI across the northeast-southwest gradient from the shoreline to a river mouth and transect ST located along the northwest-southeast shoreline. Then, this study applied the Stack Profile Tool in ArcGIS Pro to extract elevation and subsidence velocities along these transect lines for profile analysis.

4. Results

4.1. InSAR-derived subsidence velocity

4.1.1. Spatiotemporal pattern of land subsidence

The LOS velocities from ALOS-1 PALSAR-1 and Sentinel-1 images are shown in Fig. 4. Positive values indicate ground motions toward the satellite (i.e., uplift) and negative values indicate ground motions away

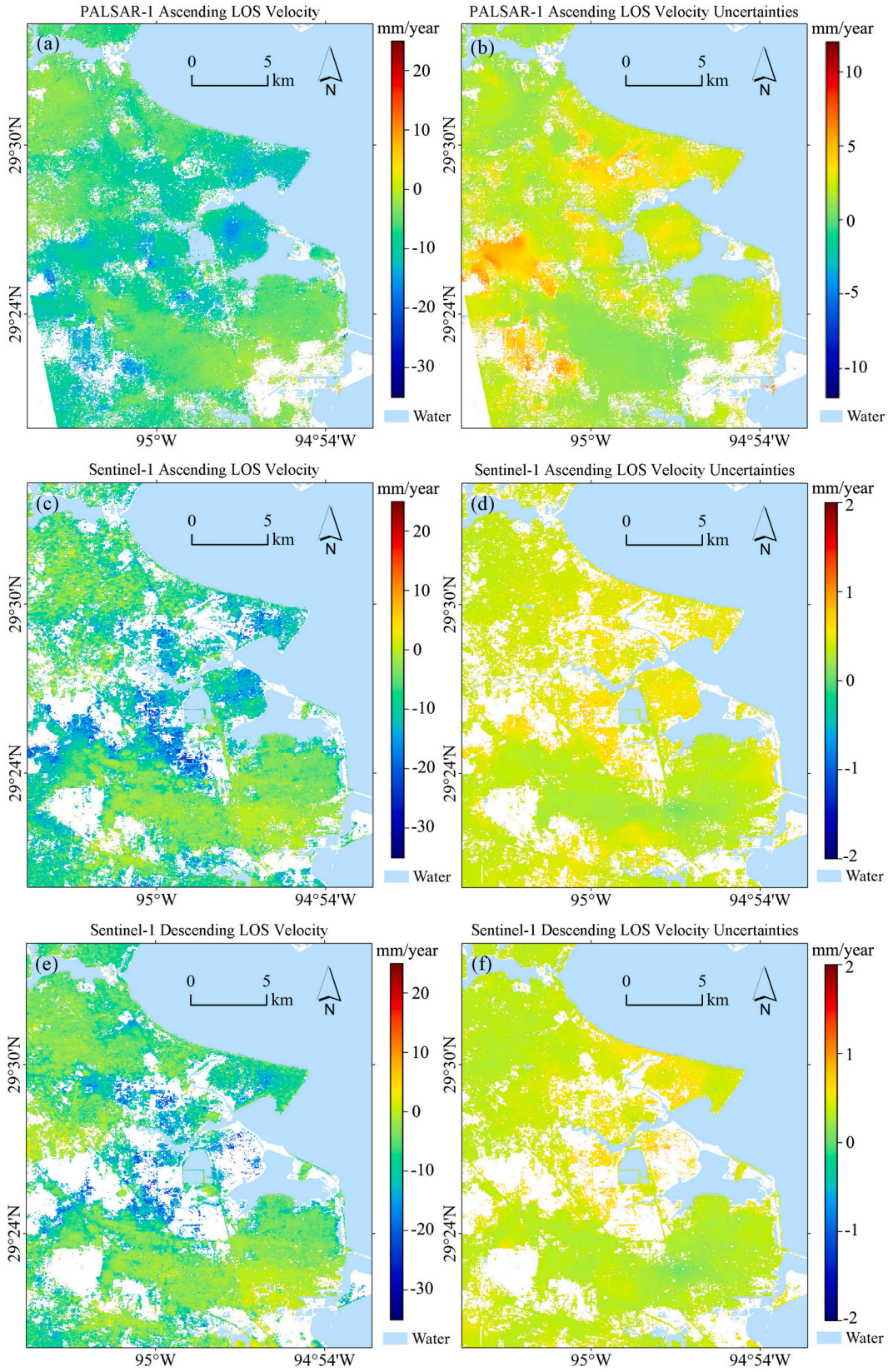

Fig. 4. LOS velocities and standard deviations derived from (a and b) PALSAR-1 ascending images (2006–2011), (c and d) Sentinel-1 Path 136 ascending images (2016–2021), and (e and f) Sentinel-1 Path 143 descending images (2016–2021).

from the satellite (i.e., subsidence). For PALSAR-1 analysis between 2006 and 2011, the LOS velocities varied from −33 to 20 mm/year (Fig. 4a) with the standard deviations of 0 to 12 mm/year (Fig. 4b). Results showed that the significant subsidence in 2006–2011 tended to continue in the next time window analyzed and with a similar magnitude. From 2016 to 2021, the LOS velocities ranged from −31 to 19 mm/year based on Sentinel-1 ascending geometry analysis (Fig. 4c) and ranged from −31 to 17 mm/year based on descending geometry analysis (Fig. 4e). The standard deviations of LOS velocities for Sentinel-1 ascending and descending geometries were smaller than 2 mm/year (Fig. 4d and f).

The velocities in the vertical direction under the assumption of zero north-south motion in 2016–2021 based on both ascending and descending Sentinel-1 results are shown in Fig. 5. For velocities in the vertical direction, positive and negative values indicate ground uplift and subsidence, respectively. This study found that the vertical velocities were up to −34 mm/year, with a spatial pattern similar to that of the LOS velocities (Fig. 4c and e). Our findings agreed with the results from a previous InSAR study in this region (Miller and Shirzaei, 2021).

4.1.2. Validation

Fig. 6 shows the validation of InSAR_derived subsidence in the vertical direction against the vertical GPS measurements, all presented in the form of accumulative depth. For the ALOS-1 PALSAR-1 results, only ascending data were available over the study area. Therefore, the vertical results transformed from LOS results using the local incidence angle were used for validation, assuming that the vertical component dominated the subsidence. For the Sentinel-1 results, the derived vertical results under the assumption of zero north-south motion (Wright et al., 2004) were compared to vertical GPS measurements. The GPS measurements agreed well with both PALSAR-1 results from 2006 to 2011 (RMSE = 7.5 mm) and Sentinel-1 results from 2016 to 2021 (RMSE =11.6 mm).

4.2. Airborne LiDAR-derived land surface difference

Here we compared the results of InSAR and airborne LiDAR over a subset of the study area that experienced substantial subsidence (Fig. 7, also marked as a blue rectangle in Fig. 1b). InSAR results (Fig. 7c and d) included some empty pixels because of the temporal coherence thresholds setting used to ensure reliable estimates. In contrast, the 1-m ground differences between 2006 and 2018 based on two temporal airborne LiDAR data covered the entire area (Fig. 7b). As airborne LiDAR measurements were in the vertical direction, LOS PALSAR-1 results-derived vertical components based on Eq. (6) (Fig. 7c) and Sentinel-1 vertical results (Fig. 7d) were used here. The PALSAR-1 results indicated a strong subsidence process (up to −22 mm/year) in 2006–2011 (Fig. 7c). The subsidence appeared to be continuing at several locations in 2016–2021 from Sentinel-1 results (Fig. 7d) when the subsidence velocities in the vertical direction were up to −25 mm/year. In the upper-right part, the vertical velocities derived from PALSAR-1 images under the assumption of no east-west and north-south motion (Fig. 7c) were larger than that from Sentinel-1 images under the assumption of no north-south motion (Fig. 7d). Groundwater use, human activities such as building construction, etc. might lead to quicker subsidence in 2006–2011 than in 2016–2021. Airborne LiDAR results revealed plenty of areas with a surface change between −0.3 to 0.1 m (Fig. 7b). Limited and scattered areas were with large surface changes (negative or positive), which were likely induced by human activities and other surface processes (for example, areas A1 and A2 highlighted in Fig. 7a). Overall, both InSAR-based analysis and airborne LiDAR measurements indicated substantial subsidence in this area. Most highly subsided areas based on InSAR analysis also showed relatively large surface changes based on airborne LiDAR measurements, between −0.1 to −0.3 m during 2006–2018 (Fig. 7). The 1-m airborne LiDAR results offered more details of the surface differences and could capture some large changes that InSAR cannot monitor.

We further conducted profile analysis along two transect lines (Fig. 7a) to evaluate the agreement and disagreement between InSAR and airborne LiDAR estimates. The transect line L1 represented the northwest-southeast direction, with the land use dominated by developed and vegetated areas. PALSAR-1 and Sentinel-1 results presented a trend similar to that of the accumulative land surface differences from the airborne LiDAR results (Fig. 8a and b). The lower subsidence velocities tended to be associated with smaller accumulative surface differences, and higher velocities aligned with greater accumulative surface differences. In particular, the airborne LiDAR results of sections BC and DE exhibited large land surface differences. The PALSAR-1 and Sentinel-1 velocities also showed high values in these sections, especially velocities from Sentinel-1 analysis (up to about −20 mm/year). The high velocities could contribute to the large subsidence, which had a good agreement with the airborne LiDAR results (Fig. 8b). Based on Google historical images, section BC was on a piece of land with some grass and almost had no change from 2006 to 2011 (Fig. 9a). This area was influenced by a pool and other activities then, confirming the great variations of Sentinel-1 subsidence velocities (Fig. 8b). Section AB subsided from both PALSAR-1 and Sentinel-1 results, whereas airborne LiDAR results presented almost no subsidence and even some uplift. Based on this multi-period information, we could infer that this segment might have an uplift in 2011–2016.

The transect line L2 represented the southwest-northeast direction. Sentinel-1 velocities trend almost fits well with the trend of land surface differences as shown in airborne LiDAR results (Fig. 8d). PALSAR-1 velocities trend of the sections starting around H fits relatively well with the land surface differences trend (Fig. 8c). Sentinel-1 analysis showed high velocities in the vertical direction over the area where airborne LiDAR obtained large surface differences. In particular, sections GH and IJ underwent larger subsidence in 2016–2021 than in 2006–2011, leading to some large subsidence in agreement with airborne LiDAR results (Fig. 8c and d). The airborne LiDAR results showed a heterogeneous pattern of surface change along section HI, agreed better with Sentinel-1 results than PALSAR-1 results. As shown in Fig. 9b, the area along the HI was mainly dominated by grassland in 2006–2011 and had a relatively homogeneous subsidence pattern accordingly (Fig. 8c). From 2016 to 2019, within the Sentinel-1 results period, the area along the HI was disturbed and/or changed by some

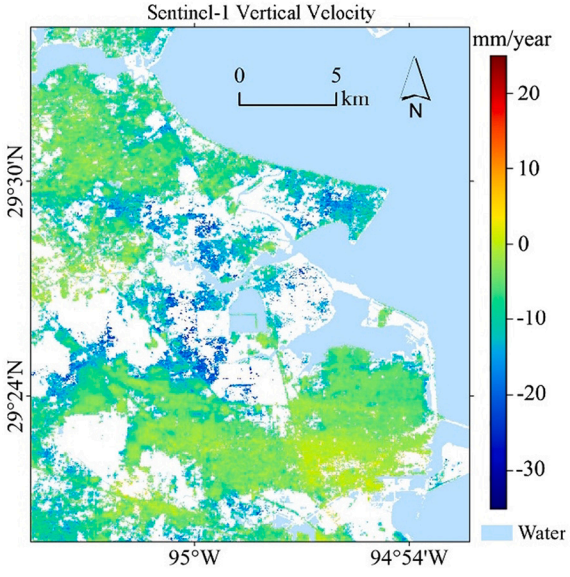

Fig. 5. The vertical components under the assumption of zero north-south motion in 2016–2021 based on Sentinel-1 ascending and descending LOS results (Fig. 4c and e).

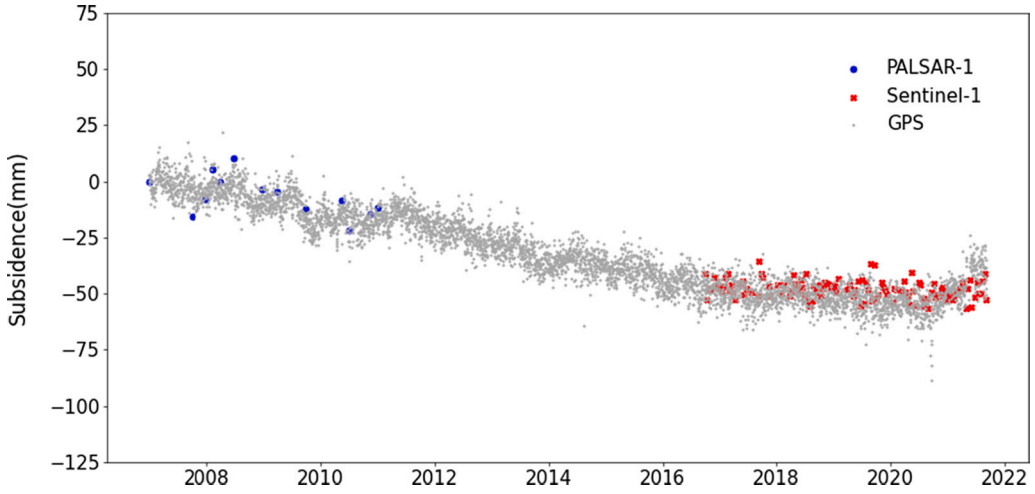

Fig. 6. Comparison of InSAR-derived cumulative subsidence to GPS measurements in the vertical direction. The location of the TXLM GPS station is shown in Fig. 1.

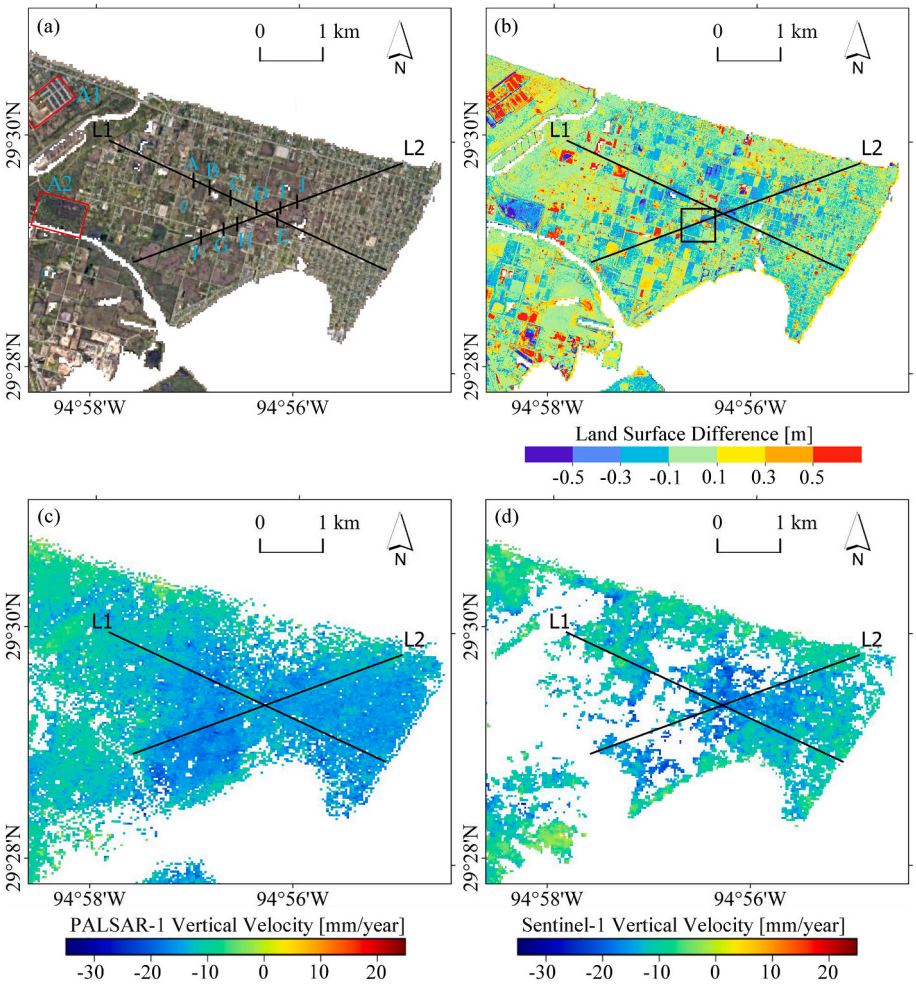

Fig. 7. Detailed subsidence pattern of a selected area: (a) a Google Earth image, (b) airborne LiDAR-derived vertical surface differences, (c) vertical components based on PALSAR-1 results (assuming no east-west and north-south motions), and (d) vertical components based on Sentinel-1 results (assuming no north-south motion). Fig. 1b shows the location of this area.

land reclamation and construction activities (Fig. 9b), leading to a heterogeneous subsidence trend as well as some substantial surface changes that could only be captured by airborne LiDAR (Fig. 8d). Sections FG subsided much faster in 2006–2011 than in 2016–2021, and the land surface change was relatively small. Overall, the land surface differences pattern derived from airborne LiDAR data between 2006 and 2018 generally agreed with InSAR-derived velocities along the selected transect lines and provided a more effective means to characterize large surface changes in areas with human activities.

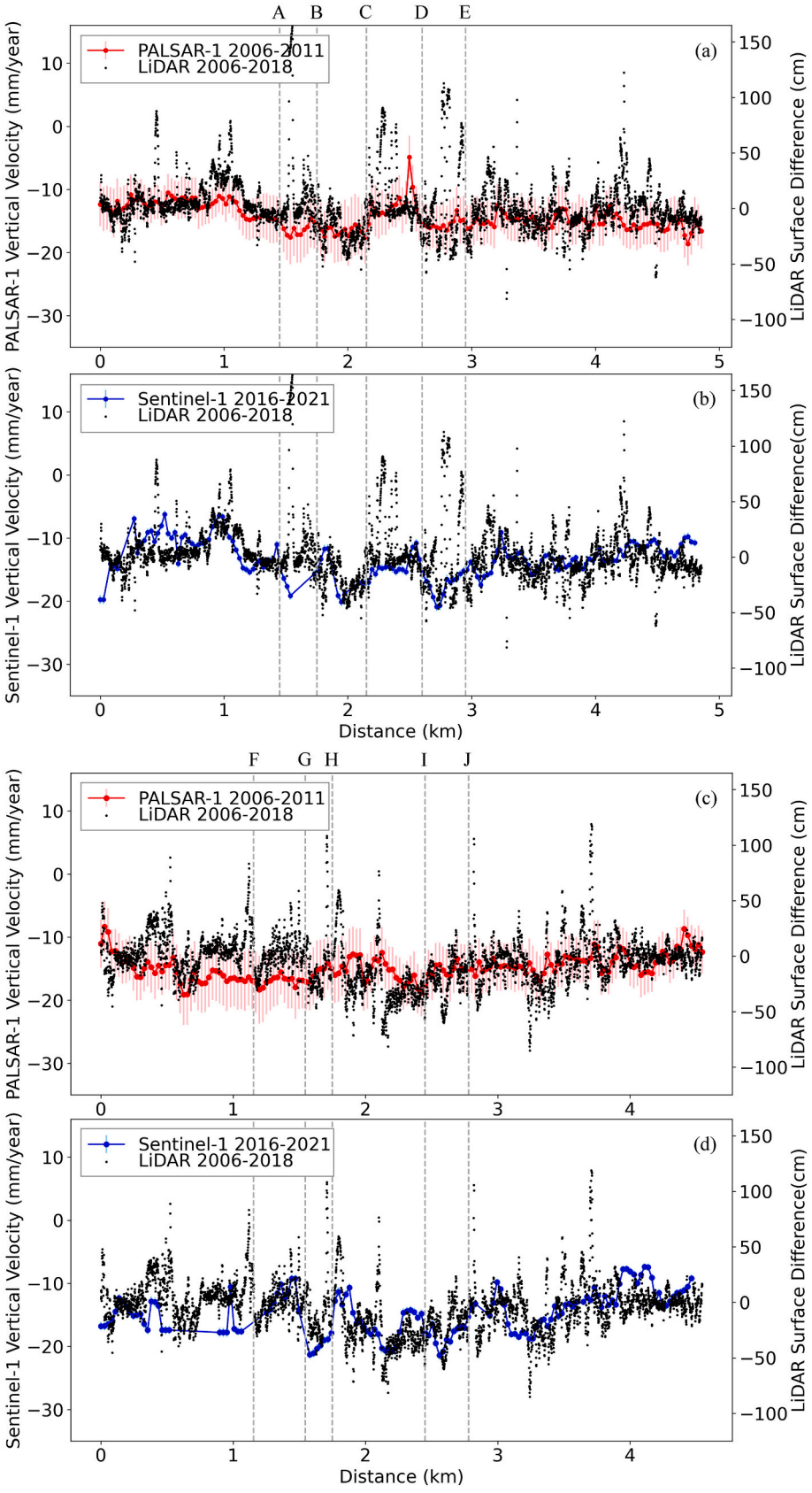

Fig. 8. Comparison of InSAR and airborne LiDAR results along transect lines L1 (a and b) and L2 (c and d). Error bars indicate standard deviations. The locations of the transect lines are shown in Fig. 7a.

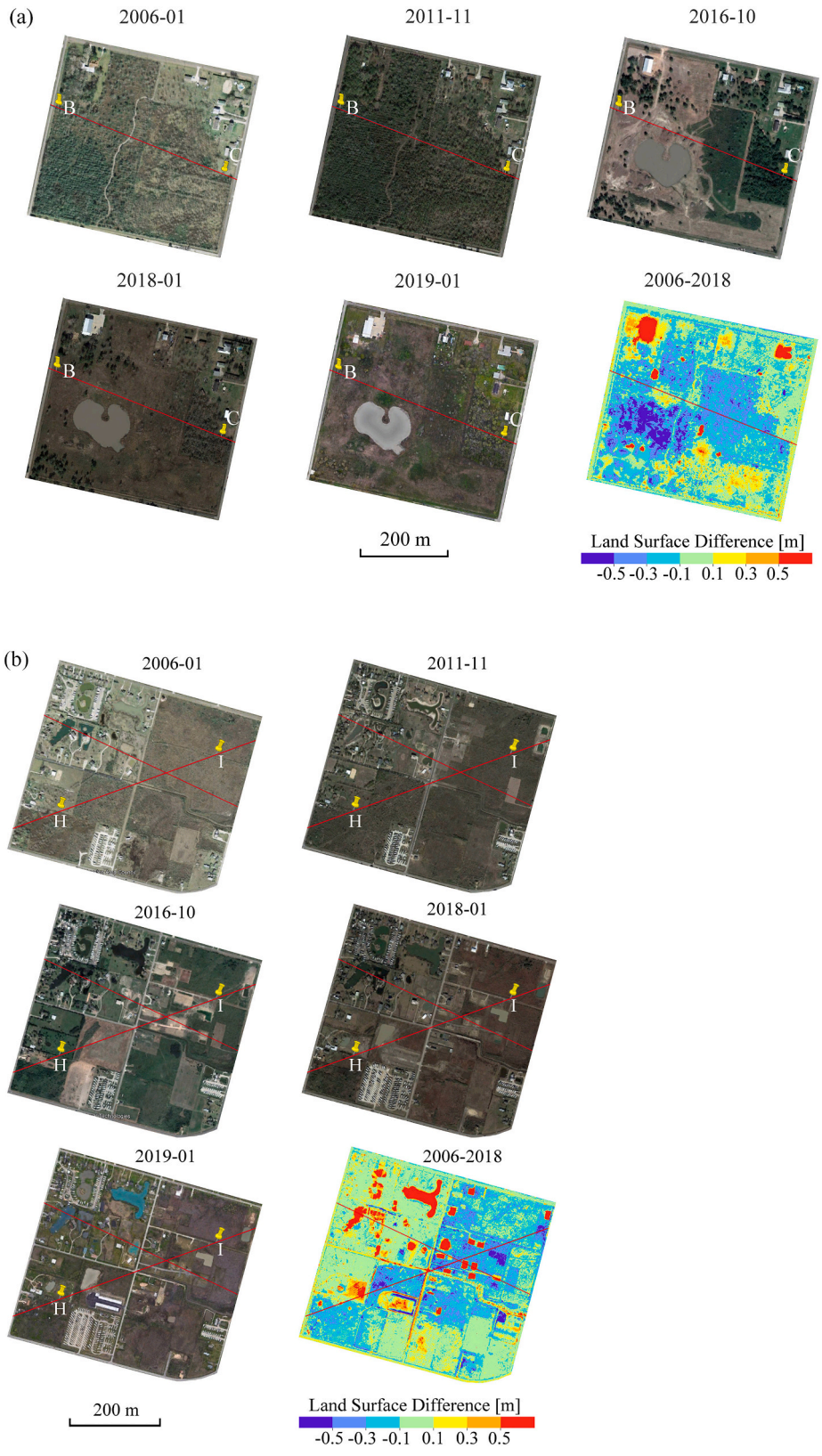

Fig. 9. Historical Google Earth images and airborne LiDAR-derived land surface differences over the selected profiles BC (a) and HI (b). The locations of BC and HI are shown in Fig. 7a. Checkpoints B, C, H, and I are denoted by yellow placemarks.

4.3. Relationships between subsidence and land cover

Based on the land cover pattern of the study area, the standard NLCD land cover categories were re-classified as developed building area, barren land, forest area, grassland area, wetland area, and open water (Fig. 10). Developed areas included four classes based on percent impervious surface coverage: open space area (<20%), low-intensity area (20%–49%), medium intensity area (50–79%), and high-intensity area (80%–100%). This study analyzed the subsidence (Fig. 4a and Fig. 5) distribution for different land cover types (Fig. 10) over the entire study area. Results showed relatively high subsidence velocities in grassland, forest, wetlands, and barren land (Fig. 11a and b). By contrast, the classes of developed areas had relatively low subsidence velocities. In particular, the developed high-intensity area was associated with the lowest subsidence velocities among all categories (Fig. 11a and b). The velocities based on Sentinel-1 analysis were more dispersed than that from PALSAR-1 analysis for each land type (Fig. 11c and d).

This study then used linear regression to explore the relationship between the percent surface imperviousness (Fig. 10) and subsidence velocities (Fig. 4a and Fig. 5) at two different scales (Fig. 12) over the entire study area. First, for all individual 30-m pixels, the least squares polynomial fit (first degree) was applied to model the relationship between the percent surface imperviousness and subsidence velocities (Fig. 12a and c). Results indicated that surface imperviousness was negatively correlated with the magnitude of subsidence velocities derived from both PALSAR-1 images ($R^2 = 0.207$) and Sentinel-1 images ($R^2 = 0.265$). Second, 30-m pixels with the same percent imperviousness value were extracted and clustered in 1% intervals from 0% to 100%, resulting in 101 clusters in which each cluster with the same imperviousness value included many pixels with various subsidence velocities. This study calculated the mean subsidence velocities for the resulted 101 clusters. Then, for the clustering results, the least squares polynomial fit (first degree) was used again to model the relationship between the percent surface imperviousness and the mean subsidence velocities (Fig. 12b and d). Results showed that the clustering procedure led to higher correlations between surface imperviousness and subsidence velocities for both PALSAR-1 ($R^2 = 0.895$) and Sentinel-1 ($R^2 = 0.937$).

5. Discussion

5.1. Improvements in existing coastal subsidence investigation

Coastal subsidence studies often have high expectations of spatial resolution and vertical accuracy to meet the requirements of various coastal studies such as flood risk analysis, shoreline erosion control, etc. InSAR works well in monitoring the gradual land subsidence with high accuracy over the coastal areas (Higgins et al., 2014). On the other hand, airborne LiDAR can monitor the land surface difference with a high spatial resolution (Jones et al., 2013). In this study, airborne LiDAR datasets contributed to a 1-m land surface differences mapping. Land surface differences detection includes the accumulation of gradual land subsidence and land displacements induced by human activities and other surface processes. The results of this study indicate the unique benefits of combining InSAR and airborne LiDAR measurements to improve the understanding of the spatiotemporal pattern of subsidence.

From the spatial perspective, InSAR analysis based on PALSAR-1 and Sentinel-1 images was constrained by its relatively low spatial resolution. However, the detailed surface changes derived from the 1-m airborne LiDAR results can contribute to a better understanding of the spatial variability of land deformation within the 30-m InSAR pixel. As demonstrated in the first example in Fig. 13, the gradual subsidence over a piece of land with some grasses was consistently captured in both InSAR and airborne LiDAR results (Fig. 13a). PALSAR-1 and Sentinel-1 results indicated main moderate subsidence rates of −0.9 to −1.5 cm/year, while airborne LiDAR results also suggested a moderate magnitude of the total surface change mianly between −0.1 to −0.3 m over 12 years. In addition to the consistent characterization of an overall moderate subsidence process, the airborne LiDAR results revealed a higher degree of spatial heterogeneity. Besides, for areas with significant surface displacements over a short time which InSAR cannot capture due to decorrelation, the additional surface change information from airborne LiDAR could contribute to the analysis at the block or even building

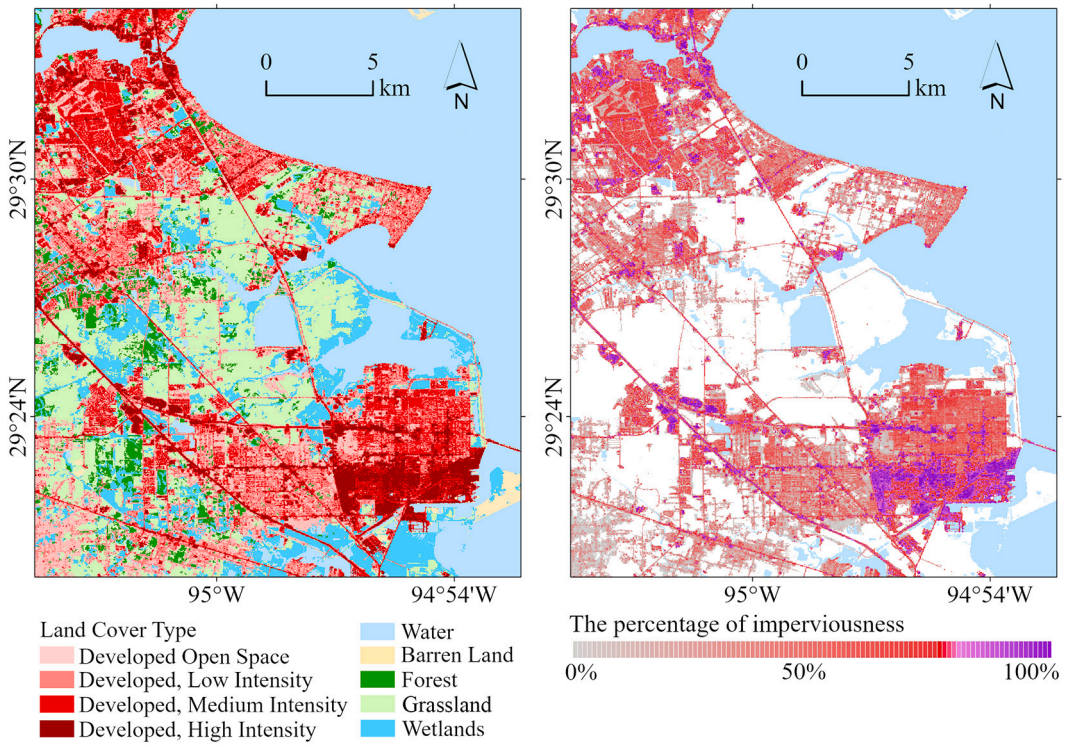

Fig. 10. Land cover of the study area based on NLCD 2019.

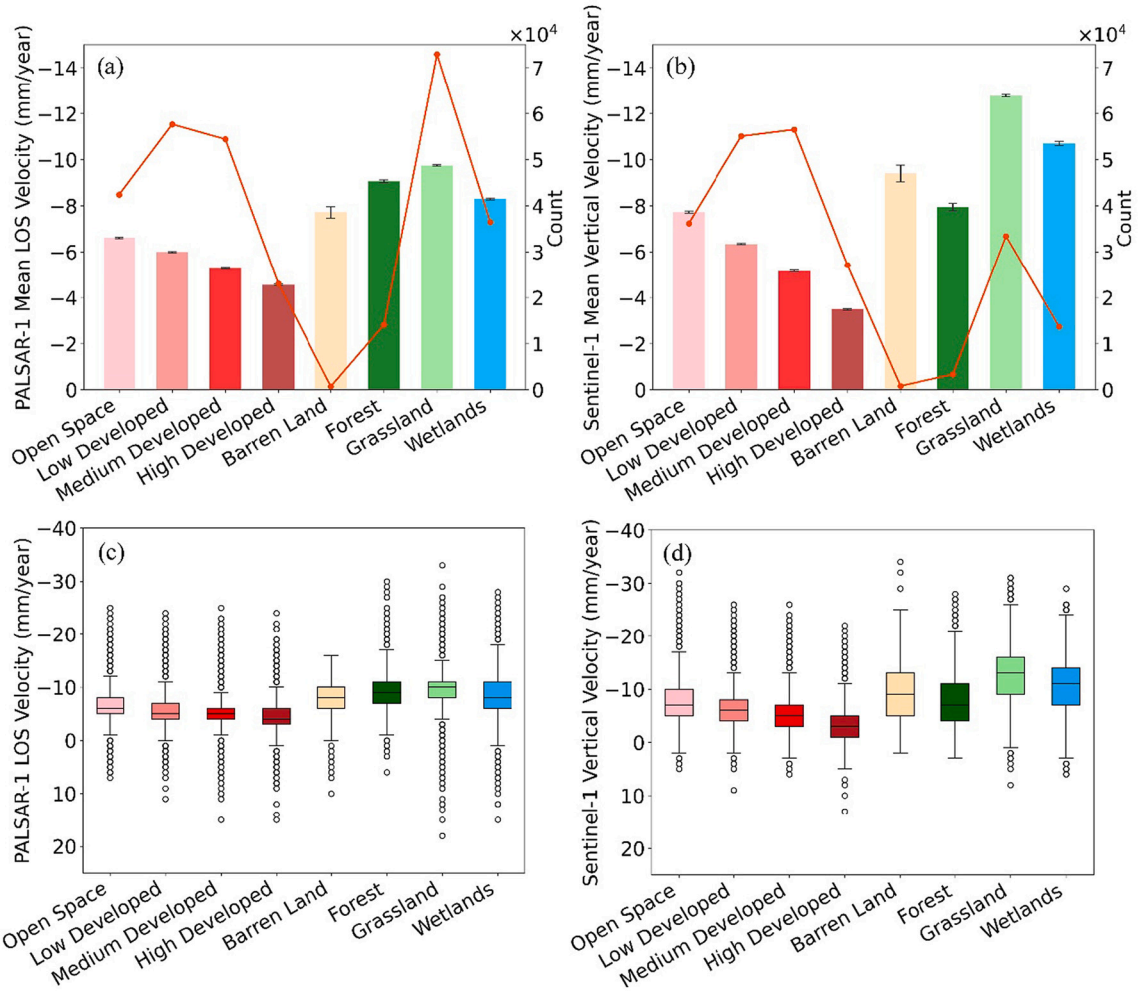

Fig. 11. PALSAR-1 mean LOS velocities (a) and Sentinel-1 mean vertical velocities (b) for different land cover types. The 95% confidence intervals are computed as 1.96 standard errors for each land type. The red line represents the number of pixels. Subplots c and d show the interquartile ranges of PALSAR-1 LOS velocities and Sentinel-1 vertical velocities for different land cover types, respectively. (For interpretation of the references to colour in this figure legend, the reader is referred to the web version of this article.)

scale, playing a critical role in high-resolution hydraulic and hydrologic simulations in coastal regions. These relatively large surface displacements occur most likely due to human activities changing the structure of the upper ground such as modifications related to roads and drainage structures construction or building foundations. The second example (Fig. 13b) illustrated a large surface deformation caused by the construction of a stormwater drainage system for a new RV parking lot. It involved some local elevation decreases due to the elevation excavation of a stormwater ditch and some local elevation increases caused by the placement of a culvert (Fig. 13b). These changes were clearly delineated in the airborne LiDAR results and obviously not associated with gradual subsidence, and they were not identifiable in the InSAR results. Overall, without the complementary high-resolution information from airborne LiDAR results, PALSAR-1 and Sentinel-1 analysis excluded important surface changes within a coarse InSAR pixel could not address significant land deformation over the small dimensions of natural and built features in a heterogeneous urban environment.

From the temporal perspective, subsidence velocities derived from PALSAR-1 and Sentinel-1 images in non-overlapping periods validated and complemented the land surface differences revealed by airborne LiDAR results and vice versa. In this study, InSAR analysis provided subsidence velocities in 2006–2011 (PALSAR-1, Fig. 7c) and 2016–2021 (Sentinel-1, Fig. 7d). Airborne LiDAR-derived land surface change estimated the total surface change between 2006 and 2018 (Fig. 7b). Our analysis showed that InSAR results and airborne LiDAR measurements fit relatively well along the selected profiles (Fig. 8). It implies that we can deduce a large land surface difference based on high PALSAR-1 and/or Sentinel-1 subsidence velocities as well as deduce high subsidence velocities from the large land surface change. The validation between high subsidence velocities and large land surface differences could be achieved. Besides, two temporal InSAR results complement the airborne LiDAR results by offering the velocities variation in the different periods. The analysis across the partially overlapping monitoring periods of airborne LiDAR, PALSAR-1, and Sentinel-1 allowed for the investigation of possible surface changes that took place within 2011–2016, i.e., the gap between the ALOS-1 and Sentinel-1 results. For example, the subsidence velocities of section AB (Fig. 7a) exceeded −15 mm/year in 2006–2011 and 2016–2021 (Fig. 8a and b). However, section AB presented limited negative land surface differences from airborne LiDAR results, which may imply some uplift between 2011 and 2016. Such partially overlapping periods of InSAR and airborne LiDAR measurements would be common in many regions, given the global availability of ALOS-1 and Sentinel-1 data. As a result, the unique advantage of including airborne LiDAR measurements could be applicable to other coastal regions.

Finally, high accuracy and resolution topography information is essential for flood risk analysis, shoreline erosion control, etc. This is particularly true for coastal plains with gentle slopes. A slight variation

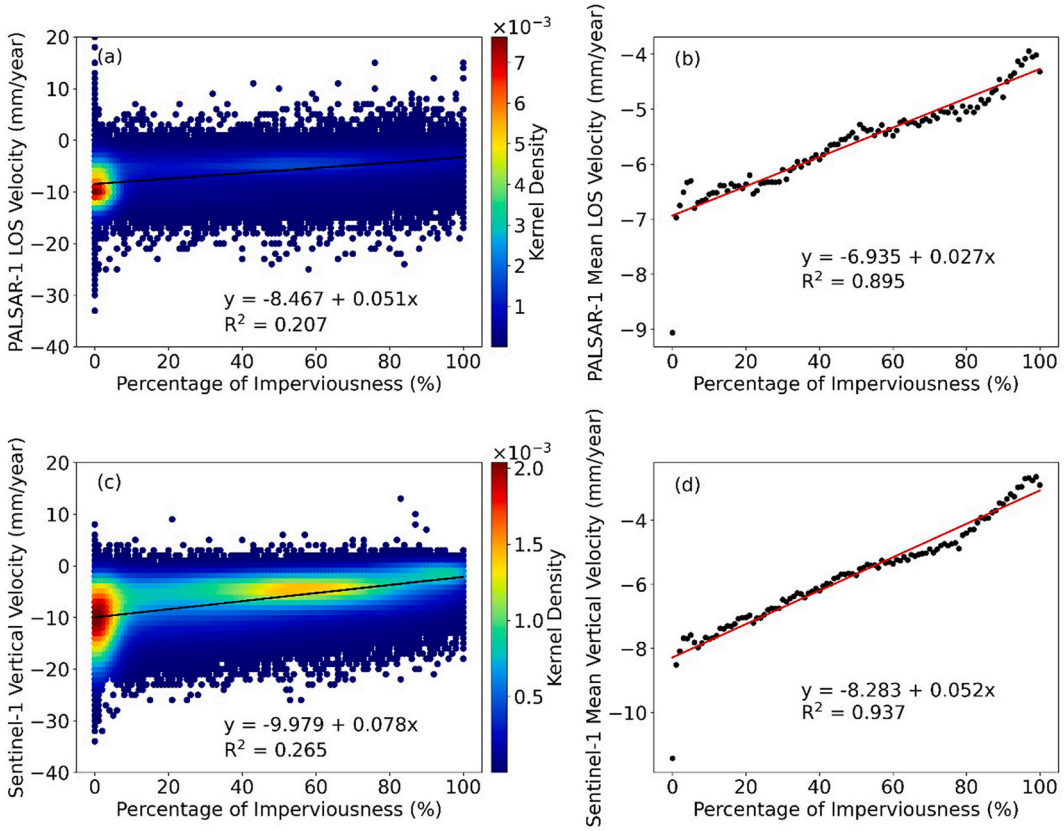

Fig. 12. Relationships between percent impervious coverage and subsidence velocities: PALSAR-1 LOS velocities at (a) the pixel level and (b) the cluster level; Sentinel-1 vertical velocities at (c) the pixel level and (d) the cluster level. Black lines (a and c) and red lines (b and d) indicate linear fit. (For interpretation of the references to colour in this figure legend, the reader is referred to the web version of this article.)

in the subsidence rates may significantly impact the calculations of flow directions and paths in hydrological and hydraulic simulations that are based on the subsidence-corrected DEMs. For such simulations in urban watersheds along the Texas Gulf Coast, to our knowledge, DEMs with spatial resolutions from 1-m to 10-m and vertical accuracies below 10 cm would be desired in most cases. Some present studies try to apply high-resolution airborne LiDAR topography to the hydrological model for improving urban flooding analysis and apply UAV-collected high-resolution images for shoreline detection (Trepekli et al., 2022). This study offers 1-m land surface change results and cm-level velocities, which will contribute to a much more robust analysis.

5.2. Limitation and potential of airborne LiDAR for coastal surface change mapping

Point positioning accuracy of airborne LiDAR is influenced by system calibration, time synchronization between system components, errors in the navigation solution (position and attitude errors), range measurement errors, etc. (May and Toth, 2007), leading to a relatively low vertical accuracy (i.e., 10–15 cm) of airborne LiDAR measurements. The limitation of low vertical accuracy results in the fact that airborne LiDAR is a less popular option for land subsidence monitoring under the conventional assumption that the total subsidence will be equal to or even smaller than the errors, as well as when the decision-makers are seeking very high accuracy. However, InSAR results have indicated substantial subsidence rates in our study area, up to −22 mm/year in 2006–2011 (Fig. 7c) and up to −25 mm/year in 2016–2021 (Fig. 7d), as well as the broader Houston region, up to −30 mm/year in 2004–2011 (Qu et al., 2015). Given such large subsidence rates, the vertical accuracy of airborne LiDAR would no longer be a constraint to decision-makers interested in identifying significant surface deformation. Our results found that most highly subsided areas from InSAR also showed relatively large surface changes from airborne LiDAR, between −0.1 m to −0.3 m during 2006–2018 (Fig. 7). The further comparison between InSAR results and airborne LiDAR results along the selected profiles revealed a very similar trend in most areas (Fig. 8). This proved the reliability of airborne LiDAR-derived results to some extent. Furthermore, our results demonstrated that airborne LiDAR monitored the land surface change from gradual land subsidence and land displacements in coastal regions. In particular, land displacements caused by human activities and other surface processes tended to have relatively large deformation over a short time which conventional InSAR methods cannot capture.

While airborne LiDAR measurements are still limited by the low vertical accuracy, few SAR images could match the spatial resolution of airborne LiDAR measurements. New satellite images (e.g., TerraSAR-X images) have improved spatial resolutions, but their coverage and availability are far from that of Sentinel-1, resulting in relatively coarse spatial resolution of InSAR analysis for lots of coastal studies. Therefore, it would be valuable to explore airborne LiDAR data when these data can be readily obtained in areas that do not have high-resolution SAR images yet. The spatial variability information of surface change derived from multi-temporal airborne LiDAR data, even if the actual measurements are not as precise as InSAR, provides invaluable higher resolution complementary information, especially for the cases with large velocities that are the most important. It will benefit a variety of coastal studies, particularly on the resilience of our coastal infrastructure systems, e.g., the design of sea walls. This is also adaptive to flooding studies that typically require high-resolution elevation information. As shown in Fig. 13b, the drainage ditch identified from the airborne LiDAR results will contribute to the flooding analysis.

High-quality airborne LiDAR data spanning a long time over the

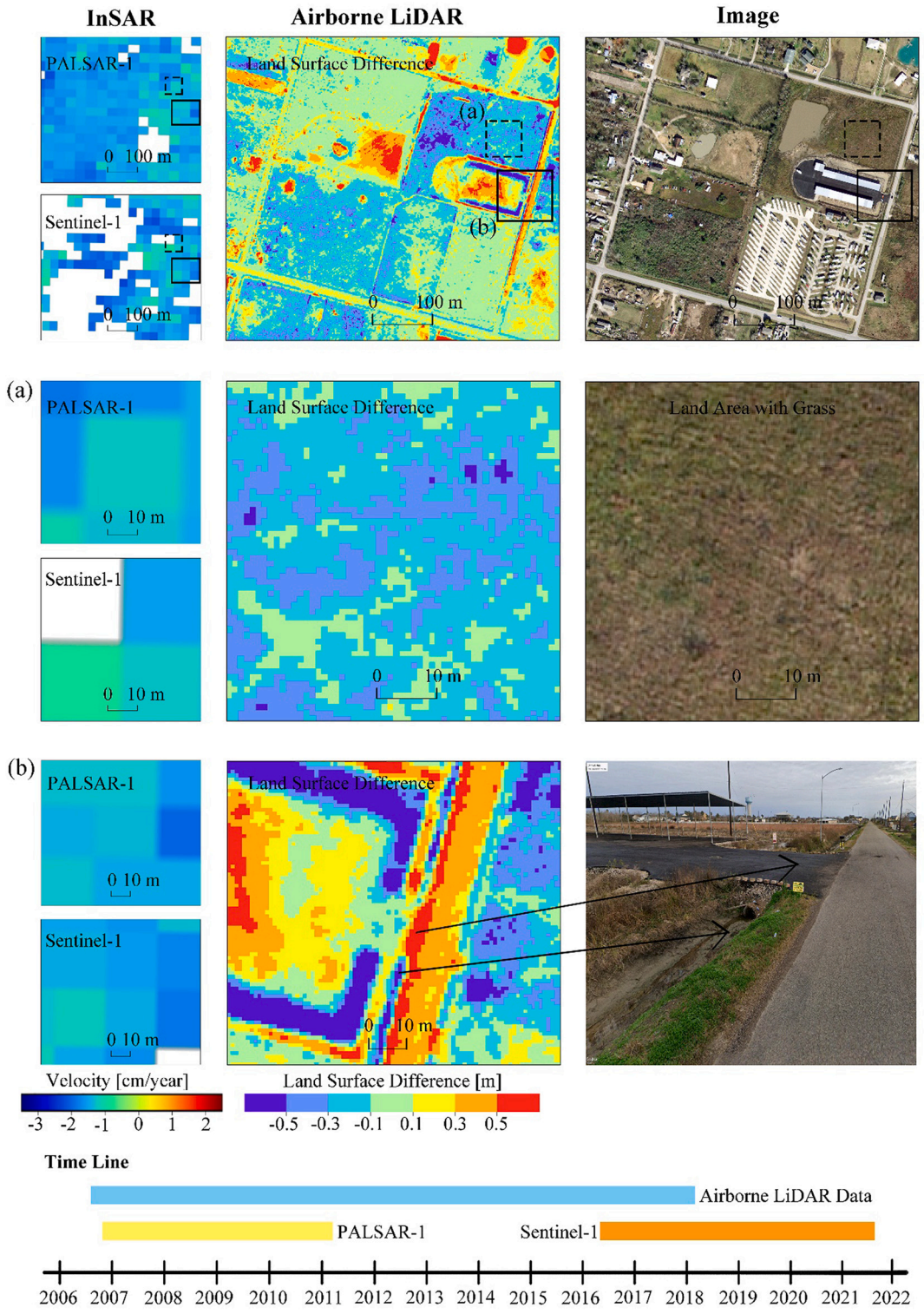

Fig. 13. Examples of the multiscale measurements in the vertical direction: (a) a grassland area (dashed box) with details presented in the second row; and (b) a developed area (solid box) with details presented in the third row. In example (a), the 0.3-m HxGN aerial image shows the landscape. In example (b), black arrows indicate the ditch and the culvert. This area is also marked in Fig. 7b.

coastal area is not widely distributed. Fortunately, more and more institutes, such as USGS, are opening their data nowadays. Airborne LiDAR data will be a good source of terrain information for surface change analysis over coastal areas with relatively large subsidence rates. Acting as complementary information, airborne LiDAR will be a potential opportunity for coastal studies.

5.3. Forest influence over the InSAR analysis

The wavelength of radar waves plays an important role in applications of InSAR over densely forested areas (Xu et al., 2021). The penetration capability of short-wavelength (3.1 cm for X-band, 5.6 cm for C-band) radar pulses is limited, which leads to the detection of the forest canopies rather than the bare land surface. As a result, decorrelation

would occur in InSAR analysis, leading to no subsidence results over the densely forested area, as shown in the forest area (Fig. 10), where few pixels (Fig. 11b) obtained subsidence results based on C-band Sentinel-1 images. Penetration capacity can be influenced by forest density as well as forest canopy height (Ni et al., 2014). Therefore, subsidence velocities over the forest area (Fig. 11b) in this study were likely measured from the ground surface over the low-density forest area. Long-wavelength (24.2 cm for L-band, 69.72 cm for P-band) radar pulses have better penetration capacity and can sense further into forest canopies. The calculated subsidence velocities in the forest area (Fig. 11a) based on L-band PALSAR-1 images had relatively large uncertainties (Fig. 4b), likely caused by low coherence (Shirzaei et al., 2020). Besides, a system bias, referred to as the fading signal, has been reported and discussed when multiple multi-looked short temporal baseline interferograms are used to overcome the rapid loss of coherence in long-term interferograms over the forest and densely vegetated areas (Ansari et al., 2021; De Luca et al., 2022; Pepe et al., 2015). This phase bias might be a further possible source of uncertainty in short-time SBAS InSAR analysis.

5.4. Subsidence and topography patterns

Topography is essential for flooding risk assessment and management over coastal regions (Miller and Shirzaei, 2021). Low-lying coastal areas are more prone to inundation. Subsidence over the low elevation coastal area potentially exacerbates the situation. In this study, subsidence velocities and elevation along the two profiles (Fig. 15a, QI, ST) over the study area were extracted (Fig. 14). Sentinel-1-derived velocities in the vertical direction were higher than PALSAR-1-derived LOS velocities in the 0–12 km section of the profile QI (Fig. 14a). The elevation was lower than 5 m in the QI section 0–12 km. Velocities for both sensors increased in QI section 15–20 km, where elevation declined nearly 3 m in a similar trend (Fig. 14a). Along with the profile QI, the low elevation area exhibited relatively high velocities, especially during the Sentinel-1 monitoring period. The elevation along the profile ST was relatively lower than QI (Fig. 14b). High velocities appeared in ~5 km, where the elevation was almost lower than 2 m. PALSAR-1 derived LOS velocities along the ST showed a similar trend to the vertical velocities from Sentinel-1 analysis. By analyzing the subsidence performance over the topographic surface, this study found that some low areas subsided at a relatively high velocity, especially in recent years, which could contribute to flood vulnerability and risk.

5.5. Subsidence along highways

Many low-lying sections of highways are susceptible to flood inundation. Land subsidence could increase their flood vulnerability. This study examined the spatial pattern of subsidence along three highways across the study area (Fig. 15). The highways were digitalized in the Google Earth image and overlaid on the airborne LiDAR-derived DEM (Fig. 15a). Changes in elevation along the highway tracks from the northwest to the southeast were illustrated in black (Fig. 15b, c, and d). Our results demonstrated that variations of PALSAR-1 LOS velocities and Sentinel-1 vertical velocities along the highway appeared to not correlate with elevation information. In particular, State Highway 6 (SH 6) underwent a high subsidence velocity (>10 mm/year) over the 0-to-5 km section and lower velocities around −5 mm/year for the rest of the track in both PALSAR-1 and Sentinel-1 results (Fig. 15b). Along Gulf Fwy, the estimated subsidence velocities appeared to be stable for the first few kilometers then double from about −5 mm/year to −10 mm/year around the 5 km mark, and then slowly increased for the rest of the track (Fig. 15c). State Highway 146 (SH 146) experienced high subsidence velocities (~15 mm/year) in the 10-to-15 km section based on Sentinel-1 and PALSAR-1 results (Fig. 15d). However, some low-lying sections of the highways underwent relatively large subsidence velocities, such as around 17 km of the SH 6 subsided up to 10 mm/year with the elevation below 2 m, around 20 km mark of Gulf Fwy subsided approximately 5–10 mm/year with elevation about 3 m, around 12 km of the SH 146 subsided approximately 15 mm/year with elevation about 3 m. Besides, Similar patterns (increasing-to-decreasing velocities along the northwest-southeast direction) were identified in the PALSAR-1 and Sentinel-1 results for all selected highways.

6. Conclusions

The study integrated SBAS InSAR, airborne LiDAR, and land cover data to investigate coastal subsidence around Eagle Point in Texas, where a high RSLR was recorded at a tide gauge station. Our results revealed that the subsidence velocities were up to −33 mm/year in the LOS direction in 2006–2011 from ALOS-1 PALSAR-1 images and up to −34 mm/year in the vertical direction in 2016–2021 from Sentinel-1 images. The low vertical accuracy of airborne LiDAR measurements has limited its application for land subsidence mapping. However, this study found that airborne LiDAR could be a complementary means to provide information on high-resolution spatial variability of coastal subsidence over fast-subsiding areas. Our study is unique in terms of using both the InSAR-derived velocities from images time series and airborne LiDAR-derived surface changes from time-lapsed observations. Comparing the InSAR results to 1-m airborne LiDAR measurements showed good agreements along the selected profiles, i.e., areas with higher subsidence velocities based on InSAR tended to have larger surface changes based on airborne LiDAR and vice versa. More importantly, the comparison revealed that airborne LiDAR results could be

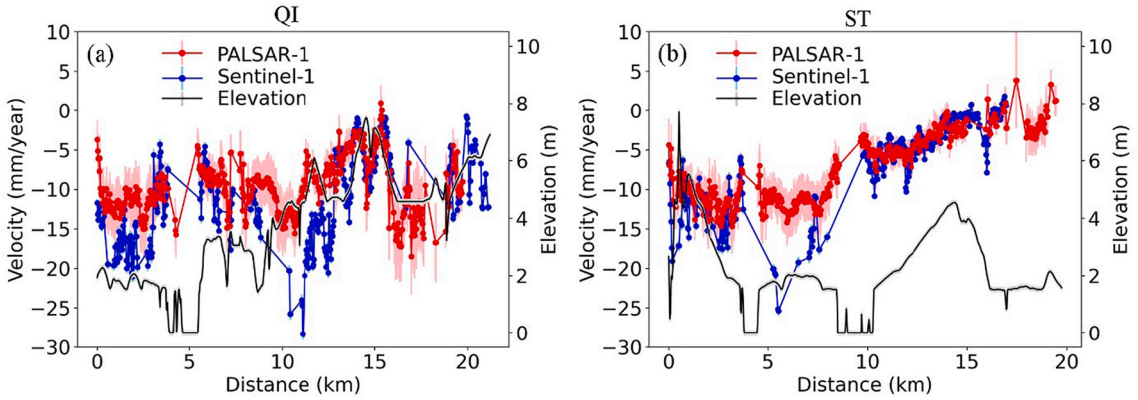

Fig. 14. PALSAR-1 LOS velocities from 2006 through 2011 (red line) with standard deviations (pink bar), Sentinel-1 vertical velocities (blue line) with standard deviations (light blue bar), and elevation (black line with vertical accuracy shown as gray bar) along the transects QI and ST. The locations of the transects are shown in Fig. 15a. (For interpretation of the references to colour in this figure legend, the reader is referred to the web version of this article.)

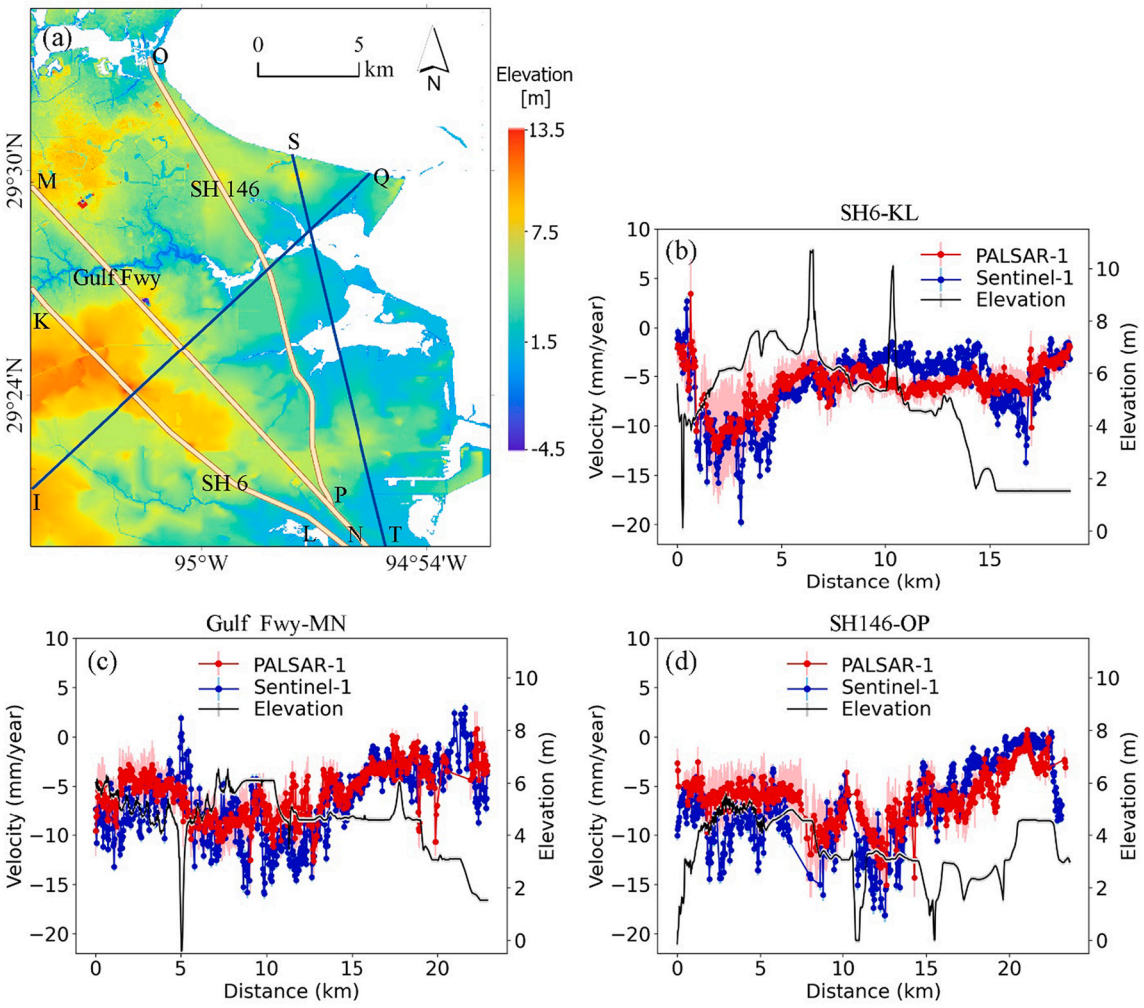

Fig. 15. (a) Digitalized highways and selected profiles over the airborne LiDAR-derived DEM. PALSAR-1 LOS velocities (red line) with standard deviations (pink bar), Sentinel-1 velocities in the vertical direction (blue line) with standard deviations (light blue bar), and elevation (black line with vertical accuracy shown as gray) over the (b) State Highway 6 (SH6)-KL, (c) Gulf Fwy-MN, and (d) State Highway 146 (SH 146)-OP. (For interpretation of the references to colour in this figure legend, the reader is referred to the web version of this article.)

complementary to InSAR results by shedding light on the subpixel variations of InSAR results and identifying significant surface changes that InSAR cannot capture. Airborne LiDAR data are not globally available like SAR images yet, but the availability of airborne LiDAR data is improving rapidly at local or regional levels in many countries. Furthermore, by incorporating land cover data, this study found that the subsidence velocities tended to be higher in forest, grassland, and wetlands than in developed urban areas. In addition, the subsidence velocities appeared to be negatively correlated with the percent impervious coverage.

Overall, the results of this study indicate that the high vertical accuracy InSAR results and the high spatial resolution airborne LiDAR results could be complementary in subsidence monitoring. An improved characterization of subsidence using both InSAR and airborne LiDAR results could provide valuable information to support a variety of coastal studies on flood vulnerability, infrastructure reliability, and erosion control. Our findings suggest the need and feasibility of multi-resolution InSAR-LiDAR fusion for mapping coastal subsidence mapping with both high accuracy and high resolution.

Credit author statement

Wen Zhong: design, data acquisition, data processing, method development, result analysis, writing, and revision; **Tianxing Chu**: design; **Philippe Tissot**: design and revision; **Zhenming Wu**: data processing and revision; **Jie Chen**: revison; **Hua Zhang**: method development, result analysis, writing, revision, and supervision.

Declaration of Competing Interest

The authors declare that they have no known competing financial interests or personal relationships that could have appeared to influence the work reported in this paper.

Data availability

Data will be made available on request.

Acknowledgments

We thank four anonymous reviewers and the associate editor for their insightful comments. This work was jointly supported by the National Science Foundation (NSF) under grants 2050986 and 2112631 to Texas A&M University-Corpus Christi, the Conrad Blucher Institute, the U.S. Department of Commerce-National Oceanic and Atmospheric Administration (NOAA) through the University of Southern Mississippi (USM) under the terms of Agreement (No. NA13NOS4000166), and the China Scholarship Council (CSC, No. 201906180081). Any opinions,

findings, conclusions, or recommendations expressed in this material are those of the authors and do not necessarily reflect the views of NSF, NOAA, USM, and CSC.

Appendix A. Supplementary data

Supplementary data to this article can be found online at https://doi.org/10.1016/j.rse.2022.113297.

References

Ansari, H., De Zan, F., Parizzi, A., 2021. Study of systematic bias in measuring surface deformation with SAR interferometry. IEEE Trans. Geosci. Remote Sens. 59, 1285–1301.

Berardino, P., Fornaro, G., Lanari, R., Sansosti, E., 2002. A new algorithm for surface deformation monitoring based on small baseline differential SAR interferograms. IEEE Trans. Geosci. Remote Sens. 40, 2375–2383.

Blewitt, G., Hammond, W.C., Kreemer, C., 2018. Harnessing the GPS data explosion for interdisciplinary science. Eos 99, 485.

Bürgmann, R., Rosen, P.A., Fielding, E.J., 2000. Synthetic aperture radar interferometry to measure Earth's surface topography and its deformation. Annu. Rev. Earth Planet. Sci. 28, 169–209.

Chen, C.W., Zebker, H.A., 2002. Phase unwrapping for large SAR interferograms: statistical segmentation and generalized network models. IEEE Trans. Geosci. Remote Sens. 40, 1709–1719.

Coplin, L.S., Galloway, D., 1999. In: Houston-Galveston, Texas. Land subsidence in the United States: US geological survey circular, pp. 35–48.

De Luca, C., Casu, F., Manunta, M., Onorato, G., Lanari, R., 2022. Comments on "Study of systematic bias in measuring surface deformation with SAR interferometry". IEEE Trans. Geosci. Remote Sens. 60, 1–5.

Dixon, T.H., Amelung, F., Ferretti, A., Novali, F., Rocca, F., Dokka, R., Sella, G., Kim, S. W., Wdowinski, S., Whitman, D., 2006. Subsidence and flooding in New Orleans. Nature 441, 587–588.

Ezer, T., Atkinson, L.P., 2014. Accelerated flooding along the U.S. East Coast: on the impact of sea-level rise, tides, storms, the Gulf stream, and the North Atlantic oscillations. Earth's Future 2, 362–382.

Fattahi, H., Amelung, F., 2015. InSAR bias and uncertainty due to the systematic and stochastic tropospheric delay. J. Geophys. Res. Solid Earth 120, 8758–8773.

Ferretti, A., Prati, C., Rocca, F., 2001. Permanent scatterers in SAR interferometry. IEEE Trans. Geosci. Remote Sens. 39, 8–20.

Fialko, Y., Simons, M., 2001. The complete (3-D) surface displacement field in the epicentral area of the 1999MW7.1 Hector mine earthquake, California, from space geodetic observations. Geophys. Res. Lett. 28, 3063–3066.

Frederikse, T., Landerer, F., Caron, L., Adhikari, S., Parkes, D., Humphrey, V.W., Dangendorf, S., Hogarth, P., Zanna, L., Cheng, L., Wu, Y.H., 2020. The causes of sea-level rise since 1900. Nature 584, 393–397.

Global Ocean Commission, 2014. From decline to recovery: a rescue package for the global ocean. Global Ocean Commission.

Higgins, S.A., Overeem, I., Steckler, M.S., Syvitski, J.P.M., Seeber, L., Akhter, S.H., 2014. InSAR measurements of compaction and subsidence in the Ganges-Brahmaputra Delta, Bangladesh. J. Geophys. Res.Earth Surf. 119, 1768–1781.

Huang, B., Shu, L., Yang, Y.S., 2012. Groundwater overexploitation causing land subsidence: hazard risk assessment using field observation and spatial modelling. Water Resour. Manag. 26, 4225–4239.

Jin, S., Homer, C., Yang, L., Danielson, P., Dewitz, J., Li, C., Zhu, Z., Xian, G., Howard, D., 2019. Overall methodology Design for the United States National Land Cover Database 2016 products. Remote Sens. 11, 2971.

Jolivet, R., Grandin, R., Lasserre, C., Doin, M.P., Peltzer, G., 2011. Systematic InSAR tropospheric phase delay corrections from global meteorological reanalysis data. Geophys. Res. Lett. 38, L17311.

Jones, B.M., Stoker, J.M., Gibbs, A.E., Grosse, G., Romanovsky, V.E., Douglas, T.A., Kinsman, N.E.M., Richmond, B.M., 2013. Quantifying landscape change in an arctic coastal lowland using repeat airborne LiDAR. Environ. Res. Lett. 8.

Leatherman, S.P., Zhang, K., Douglas, B.C., 2000. Sea level rise shown to drive coastal erosion. Eos, Trans. Am. Geophys. Union 81, 55–57.

Liu, Y., Li, J., Fasullo, J., Galloway, D.L., 2020. Land subsidence contributions to relative sea level rise at tide gauge Galveston pier 21, Texas. Sci. Rep. 10, 1–11.

May, N.C., Toth, C.K., 2007. In: Point positioning accuracy of airborne LiDAR systems: a rigorous analysis. International Archives of Photogrammetry, Remote Sensing and Spatial Information Sciences, Munich, Germany, pp. 19–21.

Meredith, M., Sommerkorn, M., Cassotta, S., Derksen, C., Ekaykin, A., Hollowed, A., Kofinas, G., Mackintosh, A., Melbourne-Thomas, J., Muelbert, M.M.C., Ottersen, G., Pritchard, H., Schuur, E.A.G., 2019. Polar regions. In: IPCC Special Report on the Ocean and Cryosphere in a Changing Climate.

Miller, M.M., Shirzaei, M., 2019. Land subsidence in Houston correlated with flooding from hurricane Harvey. Remote Sens. Environ. 225, 368–378.

Miller, M.M., Shirzaei, M., 2021. Assessment of future flood hazards for southeastern Texas: synthesizing subsidence, sea-level rise, and storm surge scenarios. Geophys. Res. Lett. 48, 2021GL092544.

Neumann, B., Vafeidis, A.T., Zimmermann, J., Nicholls, R.J., 2015. Future coastal population growth and exposure to sea-level rise and coastal flooding-a global assessment. PLoS One 10, e0118571.

Ni, W., Zhang, Z., Sun, G., Guo, Z., He, Y., 2014. The penetration depth derived from the synthesis of ALOS/PALSAR InSAR data and ASTER GDEM for the mapping of forest biomass. Remote Sens. 6, 7303–7319.

Okyay, U., Telling, J., Glennie, C.L., Dietrich, W.E., 2019. Airborne lidar change detection: an overview of earth sciences applications. Earth Sci. Rev. 198.

Pepe, A., Yang, Y., Manzo, M., Lanari, R., 2015. Improved EMCF-SBAS processing chain based on advanced techniques for the noise-filtering and selection of small baseline multi-look DInSAR interferograms. IEEE Trans. Geosci. Remote Sens. 53, 4394–4417.

Qu, F., Lu, Z., Zhang, Q., Bawden, G.W., Kim, J.-W., Zhao, C., Qu, W., 2015. Mapping ground deformation over Houston-Galveston, Texas using multi-temporal InSAR. Remote Sens. Environ. 169, 290–306.

Rosen, P.A., Gurrola, E., Sacco, G.F., Zebker, H., 2012. The InSAR scientific computing environment. In: EUSAR 2012; 9th European conference on synthetic aperture radar. VDE, pp. 730–733.

Schuerch, M., Spencer, T., Temmerman, S., Kirwan, M.L., Wolff, C., Lincke, D., McOwen, C.J., Pickering, M.D., Reef, R., Vafeidis, A.T., Hinkel, J., Nicholls, R.J., Brown, S., 2018. Future response of global coastal wetlands to sea-level rise. Nature 561, 231–234.

Shirzaei, M., Freymueller, J., Törnqvist, T.E., Galloway, D.L., Dura, T., Minderhoud, P.S. J., 2020. Measuring, modelling and projecting coastal land subsidence. Nat. Rev. Earth Environ. 2, 40–58.

Trepekli, K., Balstrøm, T., Friborg, T., Fog, B., Allotey, A.N., Kofie, R.Y., Møller-Jensen, L., 2022. UAV-borne, LiDAR-based elevation modelling: a method for improving local-scale urban flood risk assessment. Nat. Hazards 1–29.

Wang, G., Turco, M., Soler, T., Kearns, T.J., Welch, J., 2017. Comparisons of OPUS and PPP solutions for subsidence monitoring in the greater Houston area. J. Surv. Eng. 143, 05017005.

Wang, H., Wright, T.J., Yu, Y., Lin, H., Jiang, L., Li, C., Qiu, G., 2012. InSAR reveals coastal subsidence in the Pearl River Delta, China. Geophys. J. Int. 191, 1119–1128.

Wickham, J., Stehman, S.V., Sorenson, D.G., Gass, L., Dewitz, J.A., 2021. Thematic accuracy assessment of the NLCD 2016 land cover for the conterminous United States. Remote Sens. Environ. 257, 112357.

Wright, T.J., Parsons, B.E., Zhong, L., 2004. Toward mapping surface deformation in three dimensions using InSAR. Geophys. Res. Lett. 31.

Xu, Y., Lu, Z., Kim, J.-W., 2021. P-band InSAR for geohazard detection over forested terrains: preliminary results. Remote Sens. 13, 4575.

Yunjun, Z., Fattahi, H., Amelung, F., 2019. Small baseline InSAR time series analysis: unwrapping error correction and noise reduction. Comput. Geosci. 133, 104331.